Journal of Applied Physics

A new approach to electrically detected magnetic resonance: Spin-dependent transient spectroscopy

Cite as: J. Appl. Phys. **132**, 115301 (2022); https://doi.org/10.1063/5.0101852
Submitted: 03 June 2022 • Accepted: 18 August 2022 • Published Online: 15 September 2022

Kenneth J. Myers, Patrick M. Lenahan, James P. Ashton, et al.

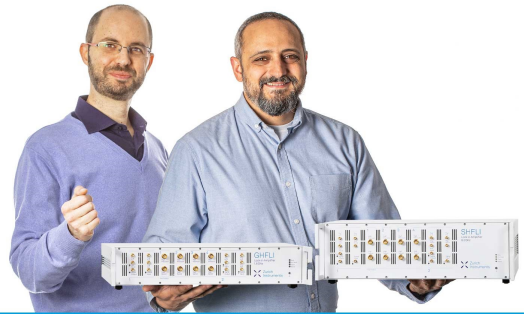

Journal of Applied Physics ARTICLE scitation.org/journal/jap

A new approach to electrically detected magnetic resonance: Spin-dependent transient spectroscopy

Cite as: J. Appl. Phys. **132**, 115301 (2022); doi: 10.1063/5.0101852
Submitted: 3 June 2022 · Accepted: 18 August 2022 ·
Published Online: 15 September 2022

Kenneth J. Myers,[1,a)] Patrick M. Lenahan,[2] James P. Ashton,[3] and Jason T. Ryan[4]

AFFILIATIONS

[1]Intercollege Graduate Degree Program in Materials Science and Engineering, The Pennsylvania State University, University Park, Pennsylvania 16802, USA
[2]Department of Engineering Science and Mechanics, The Pennsylvania State University, University Park, Pennsylvania 16802, USA
[3]High Frequency Technology Center, Keysight Technologies, 1400 Fountaingrove Pkwy, Santa Rosa, California 95403, USA
[4]Alternative Computing Group, National Institute of Standards and Technology, 100 Bureau Drive, Gaithersburg, Maryland 20899, USA

[a)]**Author to whom correspondence should be addressed:** k.j.myers5579@gmail.com

ABSTRACT

Electrically detected magnetic resonance (EDMR) is arguably the most sensitive method available to study electrically active point defects in semiconductor devices. Most EDMR studies have utilized spin-dependent recombination current and, thus, require p–n junctions or a photoconductive structure. Some time ago, Chen and Lang proposed and demonstrated EDMR via spin-dependent deep level transient spectroscopy in metal–oxide–semiconductor capacitors. We report on a similar and significantly simpler technique: spin-dependent transient spectroscopy (SDTS). We show that the sensitivity of this technique is independent of the resonance field and frequency. Through capacitance–voltage analysis, combined with our SDTS results, this technique can (crudely) provide information about the density of states of defects with a broad distribution of energy levels. In addition, we show that SDTS can be readily adapted to near-zero-field magnetoresistance effect measurements.

I. INTRODUCTION

Since its inception, electron paramagnetic resonance (EPR) has been one of the only methods for identifying the physical and chemical nature of point defects in semiconductors and insulators.[1–9] Although conventional EPR is an extremely powerful technique for relatively large samples (a few cubic millimeters or larger), it does not have the sensitivity to observe performance limiting defects within nano- or micro-electronic devices as it has a sensitivity of about 10×10^9 paramagnetic defects. The sensitivity limitations of EPR at the device level can be overcome with electrically detected magnetic resonance (EDMR).[10,11] EDMR has been utilized on a wide range of device structures, such as p–n junctions,[12,13] metal–oxide–semiconductor (MOS) capacitors,[14] bipolar junction transistors,[13] MOS field effect transistors,[15–21] multi-gate field effect transistors,[22,23] solar cells,[24] and resistive random-access memories.[25] A number of techniques have been created in order to target their various electrically active regions, including spin-dependent trap assisted tunneling (SDTAT),[25–27] gated diode recombination,[19,20,28] spin-dependent charge pumping,[18,23,29,30] and the bipolar amplification effect.[15,31,32] These studies demonstrate the capabilities of EDMR for studying the physical and chemical nature of defects in semiconducting and insulating devices.

In this study, we have adapted methodologies of deep level transient spectroscopy (DLTS)[33] and current-transient DLTS[34–36] to EDMR in MOS capacitors. In the simplest case, a voltage pulse is first applied to the gate, which brings the semiconductor/dielectric interface into accumulation. Minority carriers are driven away, and any occupied interface defect states are emptied. Next, the gate voltage is pulsed such to bring the device into depletion or weak inversion. At this point, a current transient is observed in the capacitor due to the motion of minority carriers back to the semiconductor/dielectric interface. Note that this process is relatively slow to reach equilibrium (of the order of microseconds) as it relies on the thermal generation of minority carriers. Carriers returning to the interface can also be trapped at the previously unoccupied

interface defects. If the carrier–interface defect capture process is spin-dependent, minority carrier capture events throughout the transient can be modified by magnetic resonance. This is true so long as the capture event involves an interface defect, which is initially paramagnetic, thereby requiring a specific carrier spin state to obey the Pauli exclusion principle. These spin-dependent events allow for the identification of the involved interface state defects as well as their energy levels via pulse voltage analysis. We call this measurement process "spin-dependent transient spectroscopy" (SDTS).

A somewhat similar method was demonstrated in the work of Chen and Lang,[37] wherein they utilized the gating methods of DLTS at the *X*-band (≈9.3 GHz) oscillating microwave frequency and the appropriate magnetic fields (≈340 mT) for EPR. We simplify this approach by removing the requirement of a secondary DLTS measurement, determining carrier capture rates and energy levels of the identified defects strictly through measurements of the time constants and response amplitudes in SDTS as a function of the semiconductor/insulator interface Fermi energy. This approach has the added advantage that it can provide a crude measure of the density of states of a defect with a wide distribution of energy levels within the bandgap. We also show that this technique is quite sensitive in both *X*-band and low-frequency (≈208 MHz) resonance measurements. This insensitivity to field and frequency has advantages in separating spin–orbit coupling effects on the distribution of *g* components from hyperfine interactions. In addition, SDTS yields a strong near-zero-field magnetoresistance (NZFMR) response. The near frequency independence of the resonance response allows us to, at least to some extent, deconvolute spin–orbit coupling and nuclear hyperfine interactions in the observed spectra.

II. EXPERIMENTAL METHODS

A brief introduction to EPR and EDMR is useful. Consider an unpaired electron completely unperturbed by its surroundings with an applied magnetic field ($\overrightarrow{B_0}$) and an oscillating field perpendicular to the applied $\overrightarrow{B_0}$. The applied magnetic field will split the energy of the two spin states of the electron. If an oscillating field of frequency ν is applied perpendicular to $\overrightarrow{B_0}$ such that

$$h\nu = g_e \mu_B B_0, \tag{1}$$

resonance can occur, effectively "flipping" the unpaired electron from one spin state to the other. Here, h is Planck's constant, g_e is the free electron's Landé *g*-factor ($g_e = 2.00232\ldots$), and μ_B is the Bohr magneton. The resonance condition is more complex in real systems, but for the purposes of this brief introduction and accounting for spin–orbit coupling as well as hyperfine interactions, the resonance condition can be expanded to

$$h\nu = g\mu_B B_0 + \sum_i m_i A_i, \tag{2}$$

where an orientation-dependent *g* tensor replaces the Landé *g*-factor of the otherwise unperturbed electron. Nuclear hyperfine interactions between electrons and the *i*th nuclei from the defect under study are expressed by a coupling constant, A_i, multiplied by the nuclear spin quantum number, m_i.

Conventional EPR is only sensitive to 10×10^9 paramagnetic defects per 0.1 mT linewidth at X-band frequencies and is thus unable to detect defects on the scale of modern transistors, which have far fewer defects. EDMR has a much higher sensitivity of about 10^3 paramagnetic defects.[38,39] In EDMR, the device under study is placed in an apparatus, which is very similar to that of a conventional EPR spectrometer. It consists of a microwave cavity, a microwave bridge, and an electromagnet fitted with a set of modulation coils. The device has leads connecting it to a voltage or current source and a monitoring system. EDMR sensitivity is very nearly independent of field and frequency, allowing for the comparison of high and very low field/frequency measurements.[10] This is an advantage in polycrystalline or amorphous samples in which one, to some extent, can deconvolute contributions of spin–orbit coupling in the range of *g* tensor components and hyperfine interactions.[40]

The resonance responses in EDMR generally stem from either spin-dependent recombination (SDR) or SDTAT. This paper focuses on a measurement closely related to SDR, and therefore, a somewhat oversimplified explanation of SDR will be given for clarity. In SDR, an electron from the conduction band or a hole from the valence band is first captured by a deep level defect, followed by the capture of an oppositely charged carrier. These carriers recombine at the defect site, forcing a recombination current. Consider the case of a dangling bond containing one unpaired electron. If an electron from the conduction band has the opposite spin of the unpaired electron in the defect, then the electron can be captured, rendering the defect diamagnetic. If they have the same spin quantum number, the capture event cannot occur because it would violate the Pauli exclusion principle. By flipping the defect spin via magnetic resonance, the previously forbidden event becomes allowed, causing a change in the recombination rate, which changes the device current. This process is the source of the SDR EDMR response. A more accurate model for SDR is provided by the seminal work of Kaplan *et al.*[10] The original work of Kaplan *et al.*[10] and subsequent modifications have provided a reasonable physical description of the SDR process. Our experiment does not precisely involve SDR; in SDR, one observes the effect of electron–hole pair recombination. In our measurements reported here, we directly observe electron capture events at paramagnetic defect sites.

As previously mentioned, the SDTS measurements described herein utilize a spin-dependent current-transient response. Consider a p-type silicon/oxide interface capacitor (the relevant band diagrams are shown in Fig. 1). Suppose that the capacitor gate voltage is initially held at a positive potential, which renders the interface region in strong inversion. Under this biasing condition, the Fermi energy is relatively close to the conduction band edge, and interface traps (P_b centers) are negatively charged and diamagnetic (the dangling bond orbital contains two electrons). Next, a negative voltage step is applied, bringing the interface region into accumulation. Due to the abundance of majority carriers, this process is relatively fast and equilibrium is reached quickly. The interface Fermi level is fairly near the valence band edge, and the P_b center interface defects are mostly positively charged and diamagnetic (the dangling bond "orbital" is empty).

Now, we pulse the gate voltage back to positive values (toward inversion) and consider the response of the interface during the

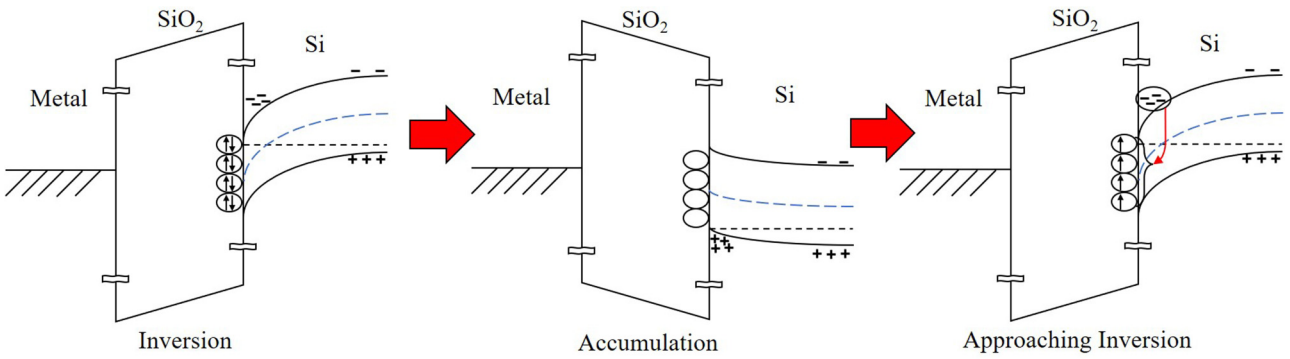

FIG. 1. Depiction of the MOS band diagrams at each step of the pulsing process.

time immediately after the pulse. There will be a current-transient response corresponding to electrons returning to the interface from the bulk. Additionally, this transient will include some of those electrons being captured at the previously unoccupied interface defects. The amphoteric interface traps (P_b centers) have two levels in the bandgap (one for each electron capture state).[5,6,41,42] The initial trapping event will involve a diamagnetic positively charged P_b center (empty dangling bond "orbital") capturing a single electron; this event *is not* spin-dependent. The second trapping event involves a now paramagnetic defect (containing a single electron in the dangling bond orbital) capturing a second electron; this event *is* spin-dependent. If both the already trapped electron and the incoming conduction band electron have the same spin quantum number, the capture event will be a forbidden process due to the Pauli exclusion principle. However, resonance can render this capture event allowed by flipping (typically) the spin state of the deep level electron. Therefore, this part of the transient response should be detectable in magnetic resonance because it will result in an increase in electron capture events.

III. EXPERIMENTAL SETUP

Capacitance vs voltage (CV) measurements in this study were made utilizing a commercially available 1 MHz oscillation frequency capacitance bridge. The CV measurements allow us to relate the bias voltage to the interface Fermi level via the Terman technique, comparing the C/C_{ox} curve of the device under study to that of an equivalent, ideal capacitor in order to extract information, such as Fermi level and interface defect density.[43] A block diagram of the transient EDMR apparatus is shown in Fig. 2. All transient data were recorded using a commercially available boxcar integrator and a waveform generator. The SDTS measurements were made at high field (≈350 mT) and frequency (≈9.8 GHz) as well as at low field (≈7.4 mT) and frequency (≈208 MHz). The high field/frequency measurements utilized an electromagnet with 4-in. pole faces, a TE_{104} microwave cavity connected to a microwave bridge, and home-made acquisition software. Low field/frequency measurements were taken on a home-built spectrometer described elsewhere,[23] in which a much smaller slowly varying magnetic field is provided by a set of custom-built Helmholtz coils, and, for spin resonance, an RF coil connected to an RF source is utilized. Devices are mounted on custom-printed boards for electrical connections. Our magnetic field modulation frequency was 210 Hz with accumulation pulse frequencies of 6.1 kHz and 14.1 kHz in order to avoid any sampling conflicts between the pulse acquisition and lock-in amplification of the SDTS response. All measurements were made at room temperature, and all displayed SDTS traces were filtered using the adaptive signal averaging method introduced by Manning *et al.*[44]

The devices utilized in our measurements were Si/SiO_2 capacitors provided by the National Institute of Standards and Technology. These MOS structures consist of a (100) p-type Si substrate ($N_A \approx 2.4 \times 10^{15}\ cm^{-3}$), 50 nm thermally oxidized SiO_2, and a 1 μm Al metal gate (including a 5 nm Ti adhesion layer). The gate area of the capacitors used in this study is approximately $7.85 \times 10^{-3}\ cm^{-2}$. Conductive paint was utilized for electrical contact to the capacitors' silicon substrate. Utilizing the Terman technique,[43] we were able to roughly estimate an interface defect density of about $6.12 \times 10^{11}\ cm^{-2}$ (equating to about 4.8×10^9 total defects within the samples under study).

IV. RESULTS AND DISCUSSION

A. EDMR and NZFMR results

In this section, we provide representative EDMR spectra for both high (*X*-band) and low (208 MHz) resonance frequencies and fields as well as the SDTS NZFMR response. For the measurements shown in this section, we utilized a pulse frequency of 14.1 kHz, an accumulation pulse width of 1 μs, an acquisition window delay of 1 μs, a window length of 3 μs, and pulse voltages of $-7.5\ V_{low}$ and $-1\ V_{high}$. The process of determining the optimal values for these parameters will be discussed in Secs. IV B–IV D. A diagram illustrating the pulse shape and the device response is shown in Fig. 3.

The high field SDTS response with the (100) Si/SiO_2 interface perpendicular and parallel to the applied magnetic field is shown in Fig. 4. This figure shows that the signal is magnetic field orientation-dependent and consistent with other studies of P_b centers on the (100) Si/SiO_2 interface.[45,46] The observed linewidth is approximately 0.8 mT wide for the perpendicular orientation and 1 mT wide for the parallel orientation, having zero-crossing

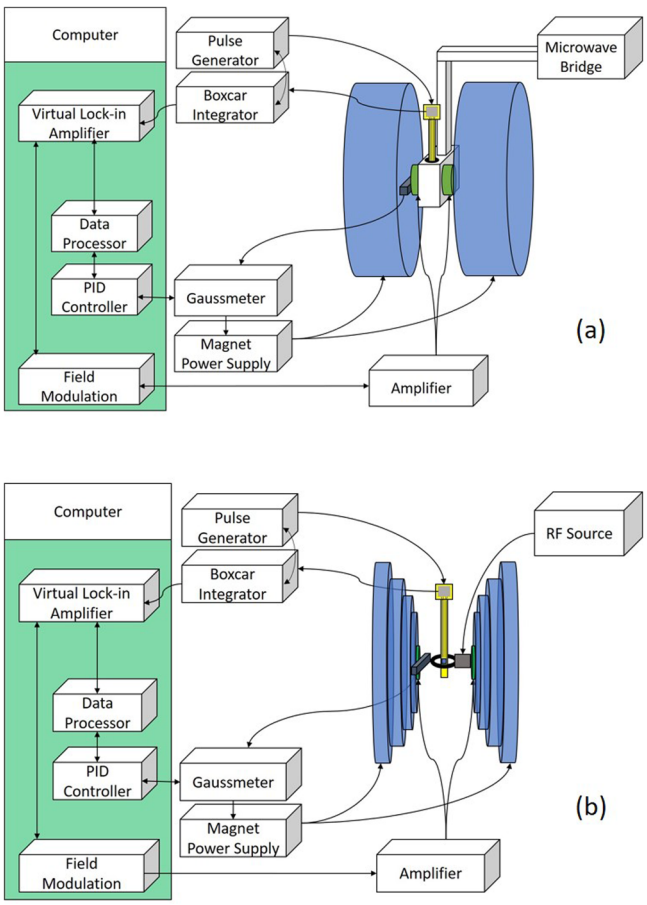

FIG. 2. Block diagram depictions of the (a) *X*-band and (b) low field EDMR spectrometers used in SDTS. The device under test is placed in (a) an microwave cavity or (b) an RF coil for the secondary oscillating field of frequency ν.

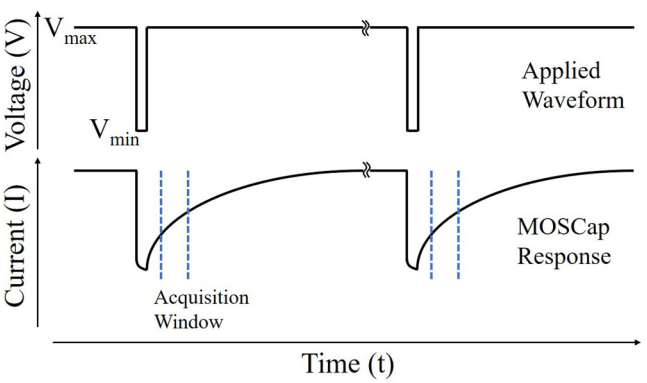

FIG. 3. A cartoon depiction of the applied waveform (top) and the corresponding device response (bottom). The dotted lines in the bottom portion represent the time window in which charge is integrated and output.

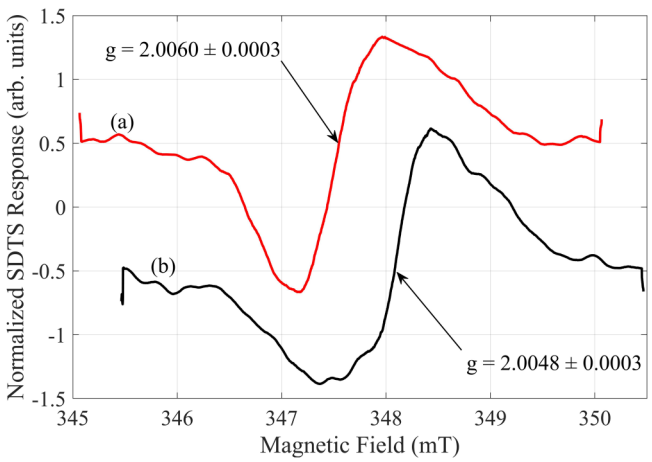

FIG. 4. SDTS signal comparison with respect to the (100) interface's orientation within the applied magnetic field at 0.3 mT field modulation. (a) was taken with the (100) plane perpendicular to the applied magnetic field and ν = 9.757 665 GHz, while (b) was taken with the (100) plane parallel to the applied magnetic field and ν = 9.763 099 GHz. The curves have been offset ±0.5 from zero for viewing purposes.

g values of 2.006 ± 0.0003 and 2.0048 ± 0.0003, respectively. These are consistent with P_b centers, known to be silicon dangling bond centers with the central silicon atom back-bonded to three other silicon atoms.[2,45,47]

In addition to the *X*-band EDMR measurements, we have performed SDTS at a low field/frequency and have also carried out the pulse sequences with no oscillating field but with a slowly varying magnetic field, which passes through zero, shown in Fig. 5. We refer to this near-zero-field behavior as the near-zero-field magnetoresistance response.[48–50] We utilize the same pulse parameters as outlined in our high frequency measurements. Figure 5(a) shows a broad magnetic field scan with a higher field modulation of 0.5 mT, while Figs. 5(b) and 5(c) utilize smaller sweep ranges with a field modulation of 0.1 mT for a higher resolution. In the low field resonance shown in Fig. 5(c), one can observe that the peak-to-peak linewidth has been slightly reduced to approximately 0.75 mT from the high field and the frequency measurement. This slight reduction in linewidth is likely due to spin–orbit effects. The peak-to-peak linewidth of the NZFMR response is about 1.4 mT wide with an inflection seen at the center of the response. This effect is described in detail in the recent literature in which the authors interpret the broad response and the inflection point as the impact of distant ^{29}Si and ^{1}H hyperfine interactions on the involved defects as the applied field approaches zero.[50,51] Our results suggest that our technique is not only applicable to conventional EDMR, but can provide some information about nuclear hyperfine effects via NZFMR.

B. Acquisition window delay analysis

The first step in determining the optimum pulse and acquisition parameters is to analyze the spin-dependent response with

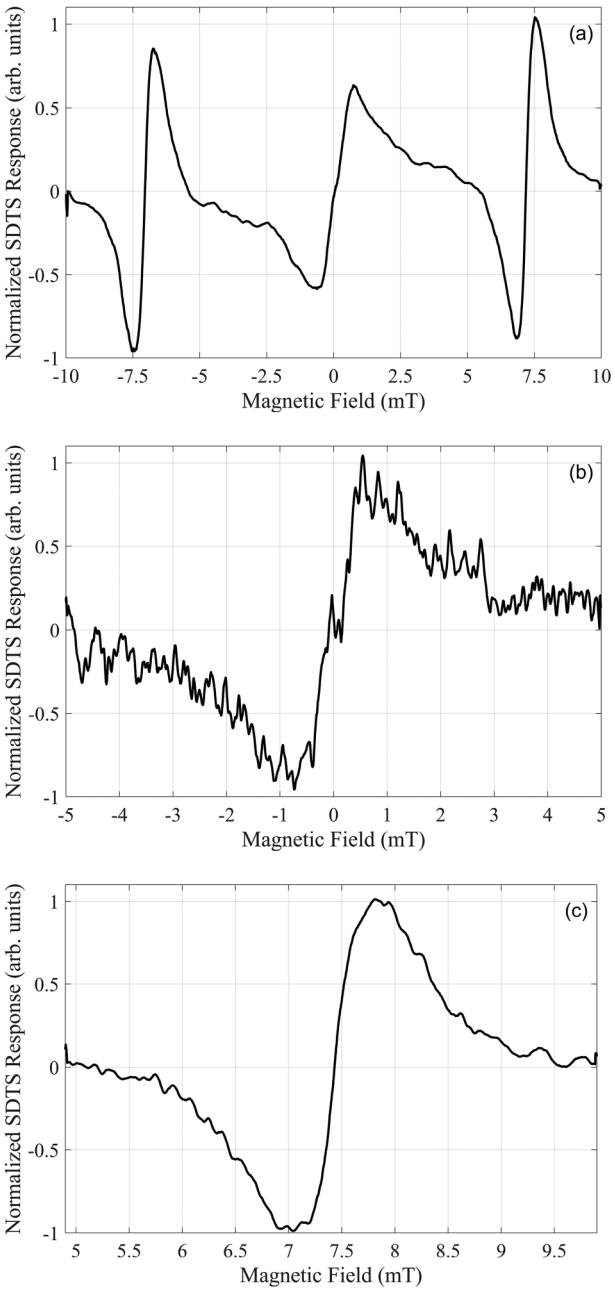

FIG. 5. (a) Low field and frequency SDTS EDMR responses (208 MHz at ±7.4 mT) and the SDTS NZFMR response (centered about 0 mT) with 0.5 mT field modulation. SDTS (b) NZFMR response with 0.1 mT field modulation and (c) low field/frequency responses with 0.1 mT field modulation.

respect to the acquisition window delay. For the measurements in this section, we utilized a pulse frequency of 6.1 kHz, a pulse width of 1 μs, an acquisition window width of 500 ns, a V_{high} of 0 V (strong inversion), and a V_{low} of −10 V (strong accumulation).

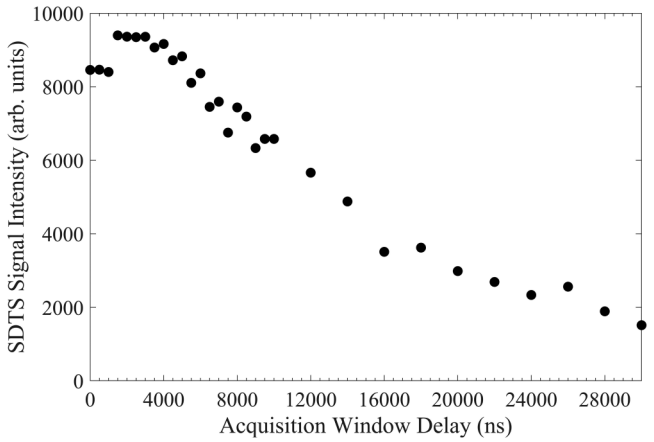

FIG. 6. Low-frequency SDTS signal intensity as a function of the acquisition window delay. The uncertainty in the data set is no greater than ±700 units.

Figure 6 shows the change in the signal intensity at low-frequency resonance as the delay on the window is varied. The acquisition window delay is then varied from 0 ns (immediately after the pulse is removed) to 30 μs in order to compare the SDTS responses. As the window delay is increased from 1.5 to 2 μs, the intensity of the response increases sharply and levels off between 2 and 3.5 μs. Afterward, the signal intensity begins to decline toward zero as the delay is increased. For the acquisition window delays of 2 and 3.5 μs, the acquisition window covers a region from 2 to 4 μs, which suggests that the highest amount of recombination at the Si/SiO_2 interface occurs with this timeframe. This is likely due to the time required for a substantial number of carriers to return to the interface and become trapped. This time would be related to the product of the capture cross sections and the density of available electrons involved in the second electron capture process.

C. Pulse voltage analysis

The next set of results that we will want to analyze are the spin-dependent responses with respect to the pulse maximum (V_{high}) and minimum (V_{low}). For the measurements in this section, we utilized a pulse frequency of 14.1 kHz, a pulse width of 1 μs, an acquisition window width of 3 μs, and an acquisition window delay of 1 μs after the pulse's trailing edge.

In order to relate the effects of the variable voltages to energy levels of our observed defects, we first compare the C/C_{ox} vs voltage curve to the biasing parameters and the spin-dependent response at 208 MHz in Fig. 7. As shown in Fig. 7(b), the amplitude of the EDMR response increases and saturates as V_{low} is swept from −3.4 to −10 V. These voltages correspond to a sweep in the Fermi energy from depletion and into strong accumulation. For this sweep, V_{high} is held constant at 0 V, bringing the Fermi energy very near the conduction band for strong inversion after each pulse. As more electrons are removed from the interface due to the V_{low} bias, more defects become available to contribute to the resonance induced response. The SDTS response is maximized

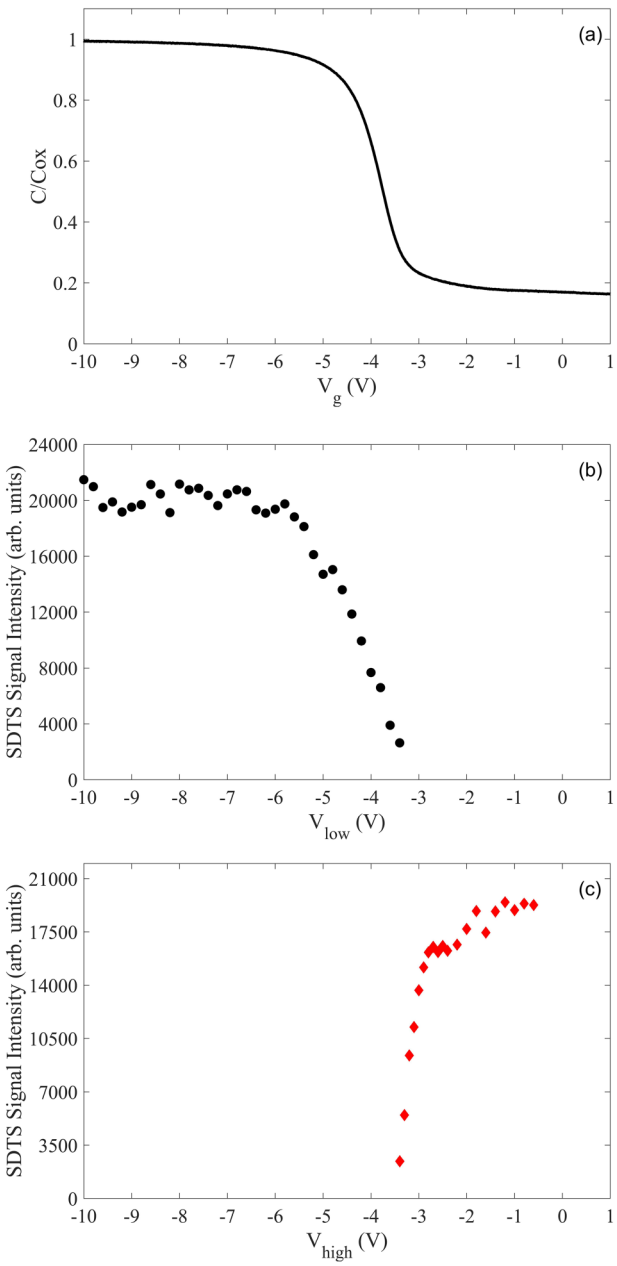

FIG. 7. (a) C/C_{ox} curve of the Si/SiO_2 capacitors used in this study. (b) Low-frequency SDTS signal intensity as a function of V_{low} with V_{high} held at 0 V. (c) Low-frequency SDTS signal intensity as a function of V_{high} with V_{low} held at −10 V. The uncertainty in the data is no greater than (b) ±1190 units and (c) ±740 units.

when the V_{low} level reaches strong accumulation at around −7 V, placing the interface Fermi energy near the valence band edge. This saturates the P_b response. As the pulse minimum is changed from weak to strong accumulation, the initial Fermi energy moves closer

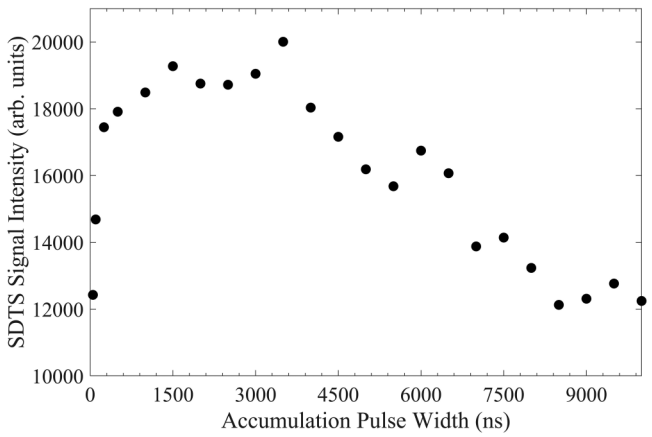

FIG. 8. Low-frequency SDTS signal intensity as a function of the accumulation pulse width. The uncertainty in the data set is no greater than ±740 units.

to the valence band. With a Fermi level very close to the valence band edge, nearly all of the defects are emptied of electrons. In this case, the SDTS should be maximized as observed in Fig. 7(b) because the number of defects participating is maximized.

It is also worth considering the case in which V_{high} is varied, while V_{low} is held in strong accumulation. Figure 7(c) shows this behavior with a V_{low} set at −10 V. As V_{high} is increased from depletion, −3.4 V, toward 0 V into inversion, the interface Fermi energy is increased from its initial value lower in the bandgap. Consequently, the SDTS amplitude increases, plateaus, and then slowly rises. Consider once again the corresponding positions of the eventual Fermi energy. After setting the voltage to $-10\ V_{low}$, the Fermi energy's position is moved toward the conduction band edge by applying V_{high}. As V_{high} is increased, the Fermi energy will shift higher up into the bandgap. If the Fermi energy fully passes through the defect energy levels, the SDTS response plateaus, indicating that the energy levels of the interface traps have been fully scanned by the pulse sequence.

D. Accumulation pulse width analysis

Last, we explored the changes in the SDTS signal intensity at a low resonance frequency as the accumulation pulse width is varied. Figure 8 shows the changes in the signal intensity as the pulse width is increased from 50 ns to 10 μs. For these measurements, we used a pulse frequency of 14.1 kHz, an acquisition window delay of 1 μs, a window length of 3 μs, and pulse voltages of $-7.5\ V_{low}$ and $-1\ V_{high}$. We observe that the signal intensity increases sharply from 50 to 500 ns, plateaus roughly between 1 and 4 μs, and then declines. These results indicate that as the pulse width is increased, a larger number of traps are being emptied and, therefore, become available for the capture process in SDTS. A further increase of the width, showing the gentle decline, may be qualitatively explained in a manner similar to that of spin-dependent charge pumping and energy transfer as described by Anders *et al.*[29] They argued that an increasing number of free carriers effectively decreases the

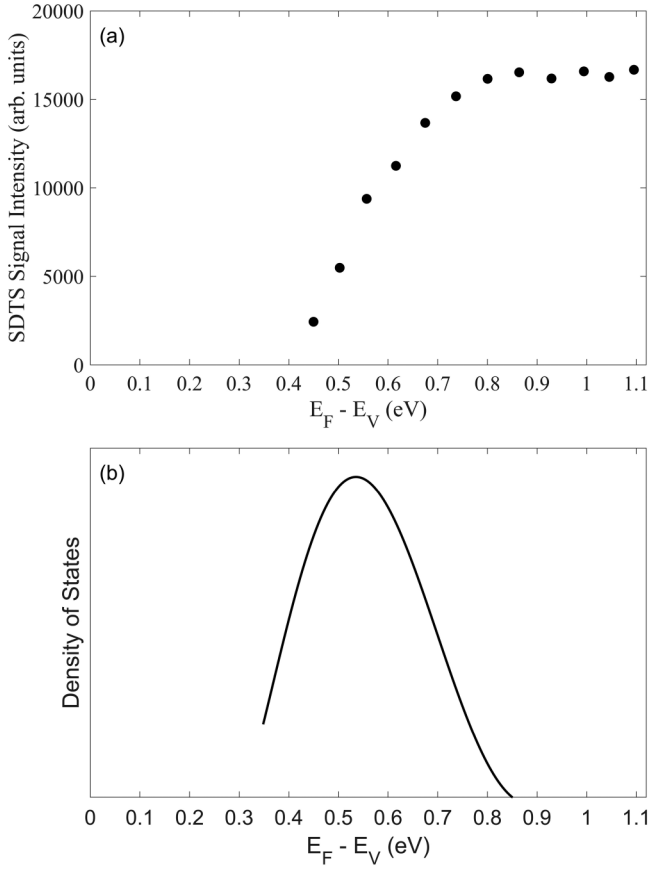

FIG. 9. (a) SDTS signal intensity as a function of Fermi energy with respect to the VBE. (b) Density of states extracted from the polynomial fitting and a subsequent derivative of (a).

paramagnetic P_b site spin-lattice relaxation times, T_1, via spin diffusion. Shorter T_1 times will reduce the size of the spin-dependent capture response. This causes the SDTS response amplitude to saturate and decay as energy is being transferred out of the observed spin system.

E. Defect energy analysis

In addition to SDTS's ability to extract the chemical and physical nature of interface traps, we can very roughly determine information about the density of states of the observed defects. The first step in this process is to analyze the C/C_{ox} curve shown in Fig. 7(a) via the Terman technique. In order to do so, we have performed a simulation using an open-source quantum mechanical CV simulation tool. Using the simulated C/C_{ox} vs surface potential, we were able to extract the relative surface potentials and corresponding Fermi energies in our C/C_{ox} measurements. Figure 9(a) shows the SDTS signal intensity against Fermi energy's distance from the valence band edge (VBE) using the same V_{high} sweep as in Fig. 7(c). As V_{high} is swept from depletion and toward inversion,

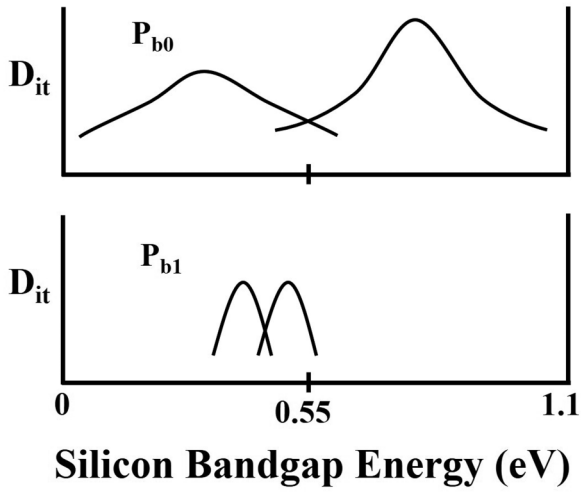

FIG. 10. Schematic representation of the density of states of the P_{bo} and P_{b1} centers in the silicon bandgap. The lower energy states represent the singly occupied P_b centers, while the higher energy states represent the doubly occupied P_b centers. Reproduced with permission from J. P. Campbell and P. M. Lenahan, Appl. Phys. Lett. **80**, 1945 (2002). Copyright 2002 AIP Publishing LLC.

the SDTS signal intensity grows rapidly as the Fermi energy is increased from 0.45 to 0.8–0.85 eV above the VBE, at which point the response saturates. The saturation in the response indicates that P_{b0} center's energy levels within the bandgap have been fully scanned by the applied waveform. This energy corresponds very well with previously reported results on the two-electron state of P_{b0} centers at the Si/SiO_2 interface.[5,6,41,52–55] Using a polynomial fit of Fig. 9(a) and taking its derivative, a very rough density of states can then be extracted, which is shown in Fig. 9(b).

A schematic illustration of the density of states is shown in Fig. 10 for comparison.[52] From the rough measure of the density of states shown in Fig. 9(b), it is observed that the states extend a few meV both above and below the midgap. We attribute the shifted distribution to two mechanisms: P_{b0} and P_{b1} energy overlap and spin-lattice relaxation effects. In general, the P_{b0} two-electron state is attributed to energy slightly above the middle of the bandgap with a broad distribution, while the P_{b1} two-electron state has a sharp distribution slightly below the middle of the gap. This could effectively skew our observed density of states toward the center of the gap. In addition, the measured density of states could be affected by spin-dependent capture rates and associated spin relaxation times, as resonance and relaxation alter the defect's capture cross section (or capture time constant).[49,56–58] Relaxation-induced dissociation through triplet state formation would act to block charge capture and would be the limiting factor in the capture cross section if the time scales of the relaxation parameters are shorter than the time scales associated with capture time constants in Si.[59] In the case of our measurements, we may be observing resonance involving longer spin rates, which could shift the density of states closer to the midgap.[58] One or both factors is likely causing

our observed density of states to appear as a broad distribution centered around the midgap.

V. CONCLUSIONS

In conclusion, we have simplified and extended Chen and Lang's spin-dependent deep level transient spectroscopy technique via SDTS. We show that one can target the interface between semiconductors and insulators in MOS capacitors, identifying electrically active interface traps, and extracting their relative capture times. Additionally, our measurements can provide a crude measure of the density of states for a defect with levels widely distributed within the bandgap. We have also shown that this SDTS can be utilized at various resonance frequencies as well as NZFMR, allowing the investigation of multiple effects, such as spin–orbit coupling and nuclear hyperfine interactions. We expect that SDTS could have advantages in other systems, such as Schottky diodes, and will explore these applications in the future.

ACKNOWLEDGMENTS

This work has been supported by the Defense Threat Reduction Agency under Grant No. HDTRA1-18-0012 and the Air Force Office of Scientific Research under Award No. FA9550-17-1-0242. The content of the information does not necessarily reflect the position or the policy of the federal government, and no official endorsement should be inferred.

AUTHOR DECLARATIONS

Conflict of Interest

The authors have no conflicts to disclose.

Author Contributions

Kenneth J. Myers: Conceptualization (lead); Formal analysis (lead); Investigation (lead); Methodology (lead); Validation (lead); Visualization (lead); Writing – original draft (lead); Writing – review & editing (supporting). **Patrick M. Lenahan:** Conceptualization (equal); Funding acquisition (lead); Project administration (lead); Resources (lead); Supervision (lead); Writing – original draft (equal); Writing – review & editing (equal). **James P. Ashton:** Conceptualization (supporting); Methodology (supporting); Resources (supporting); Writing – review & editing (equal). **Jason T. Ryan:** Formal analysis (supporting); Resources (equal); Writing – review & editing (equal).

DATA AVAILABILITY

The data that support the findings of this study are available from the corresponding author upon reasonable request.

REFERENCES

[1]W. Gordy, *Theory and Applications of Electron Spin Resonance* (John Wiley & Sons, Inc., New York, 1980).
[2]Y. Nishi, Jpn. J. Appl. Phys. **10**, 52 (1971).
[3]E. H. Poindexter, P. J. Caplan, B. E. Deal, and R. R. Razouk, J. Appl. Phys. **52**, 879 (1981).
[4]P. J. Caplan, E. H. Poindexter, B. E. Deal, and R. R. Razouk, J. Appl. Phys. **50**, 5847 (1979).
[5]P. M. Lenahan and P. V. Dressendorfer, J. Appl. Phys. **55**, 3495 (1984).
[6]P. M. Lenahan and P. V. Dressendorfer, Appl. Phys. Lett. **41**, 542 (1982).
[7]G. D. Watkins and J. W. Corbett, Phys. Rev. **121**, 1001 (1961).
[8]G. D. Watkins and J. W. Corbett, Phys. Rev. **134**, A1359 (1964).
[9]G. D. Watkins and J. W. Corbett, Phys. Rev. **138**, A543 (1965).
[10]D. Kaplan, I. Solomon, and N. F. Mott, J. Phys. Lett. **39**, 51 (1978).
[11]D. J. Lepine, Phys. Rev. B **6**, 436 (1972).
[12]I. Solomon, Solid State Commun. **20**, 215 (1976).
[13]C. J. Cochrane, P. M. Lenahan, and A. J. Lelis, Appl. Phys. Lett. **90**, 123501 (2007).
[14]J. T. Ryan, P. M. Lenahan, A. T. Krishnan, and S. Krishnan, Appl. Phys. Lett. **95**, 103503 (2009).
[15]J. P. Ashton, P. M. Lenahan, D. J. Lichtenwalner, A. J. Lelis, and M. A. Anders, in *2019 IEEE International Reliability Physics Symposium* (IEEE, 2019), pp. 1–5.
[16]M. A. Anders, P. M. Lenahan, C. J. Cochrane, and A. J. Lelis, IEEE Trans. Electron Devices **62**, 301 (2015).
[17]J. P. Campbell, P. M. Lenahan, A. T. Krishnan, and S. Krishnan, J. Appl. Phys. **103**, 044505 (2008).
[18]M. Hori and Y. Ono, Phys. Rev. Appl. **11**, 064064 (2019).
[19]G. Kawachi, C. F. O. Graeff, M. S. Brandt, and M. Stutzmann, Jpn. J. Appl. Phys. **36**, 121 (1997).
[20]T. Umeda, K. Esaki, R. Kosugi, K. Fukuda, T. Ohshima, N. Morishita, and J. Isoya, Appl. Phys. Lett. **99**, 142105 (2011).
[21]F. V. Sharov, S. J. Moxim, G. S. Haase, D. R. Hughart, and P. M. Lenahan, IEEE Trans. Nucl. Sci. **69**, 208 (2022).
[22]K. J. Myers, R. J. Waskiewicz, P. M. Lenahan, and C. D. Young, IEEE Trans. Nucl. Sci. **66**, 405 (2019).
[23]K. J. Myers, P. M. Lenahan, B. C. Bittel, and I. Meric, in *2019 IEEE International Integrated Reliability Workshop* (IEEE, 2019), pp. 1–4.
[24]K. Lips and W. Fuhs, J. Appl. Phys. **74**, 3993 (1993).
[25]D. J. McCrory, P. M. Lenahan, D. M. Nminibapiel, D. Veksler, J. T. Ryan, and J. P. Campbell, IEEE Trans. Nucl. Sci. **65**, 1101 (2018).
[26]S. J. Moxim, J. P. Ashton, P. M. Lenahan, M. E. Flatte, N. J. Harmon, and S. W. King, IEEE Trans. Nucl. Sci. **67**, 228 (2020).
[27]J. H. Stathis, Appl. Phys. Lett. **68**, 1669 (1996).
[28]D. J. Fitzgerald and A. S. Grove, Surf. Sci. **9**, 347 (1968).
[29]M. A. Anders, P. M. Lenahan, and A. J. Lelis, J. Appl. Phys. **122**, 234503 (2017).
[30]B. C. Bittel, P. M. Lenahan, J. T. Ryan, J. Fronheiser, and A. J. Lelis, Appl. Phys. Lett. **99**, 083504 (2011).
[31]T. Aichinger and P. M. Lenahan, Appl. Phys. Lett. **101**, 083504 (2012).
[32]J. P. Ashton, S. J. Moxim, A. D. Purcell, P. M. Lenahan, and J. T. Ryan, J. Appl. Phys. **130**, 134501 (2021).
[33]D. V. Lang, J. Appl. Phys. **45**, 3023 (1974).
[34]J. A. Borsuk and R. M. Swanson, IEEE Trans. Electron Devices **27**, 2217 (1980).
[35]N. M. Johnson, D. K. Biegelsen, and M. D. Moyer, J. Vac. Sci. Technol. **19**, 390 (1981).
[36]T. J. Tredwell and C. R. Viswanathan, Solid State Electron. **23**, 1171 (1980).
[37]M. C. Chen and D. V. Lang, Phys. Rev. Lett. **51**, 427 (1983).
[38]G. Kawachi, C. F. O. Graeff, M. S. Brandt, and M. Stutzmann, Phys. Rev. B **54**, 7957 (1996).
[39]M. Stutzmann, M. S. Brandt, and M. W. Bayerl, J. Non-Cryst. Solids **266–269**, 1 (2000).
[40]M. J. Mutch, P. M. Lenahan, and S. W. King, Appl. Phys. Lett. **109**, 062403 (2016).
[41]G. J. Gerardi, E. H. Poindexter, P. J. Caplan, and N. M. Johnson, Appl. Phys. Lett. **49**, 348 (1986).
[42]P. M. Lenahan and P. V. Dressendorfer, J. Appl. Phys. **54**, 1457 (1983).
[43]L. M. Terman, Solid State Electron. **5**, 285 (1962).

[44]B. R. Manning, C. J. Cochrane, and P. M. Lenahan, Rev. Sci. Instrum. **91**, 033106 (2020).
[45]Y. Y. Kim and P. M. Lenahan, J. Appl. Phys. **64**, 3551 (1988).
[46]A. Stesmans, B. Nouwen, and V. V. Afanas'ev, Phys. Rev. B **58**, 15801 (1998).
[47]Y. Nishi, K. Tanaka, and A. Ohwada, Jpn. J. Appl. Phys. **11**, 85 (1972).
[48]C. J. Cochrane and P. M. Lenahan, J. Appl. Phys. **112**, 123714 (2012).
[49]N. J. Harmon, J. P. Ashton, P. M. Lenahan, and M. E. Flatté, arXiv:2008.08121v1 [cond-mat.mtrl-sci] (2020).
[50]E. B. Frantz, N. J. Harmon, S. R. McMillan, S. J. Moxim, M. E. Flatté, and P. M. Lenahan, J. Appl. Phys. **128**, 124504 (2020).
[51]E. B. Frantz, D. J. Michalak, N. J. Harmon, E. M. Henry, M. E. Flatté, S. W. King, J. S. Clarke, and P. M. Lenahan, Appl. Phys. Lett. **119**, 184101 (2021).
[52]J. P. Campbell and P. M. Lenahan, Appl. Phys. Lett. **80**, 1945 (2002).
[53]T. Tsuchiya and P. M. Lenahan, Jpn. J. Appl. Phys. **56**, 031301 (2017).
[54]J. T. Ryan, L. C. Yu, J. H. Han, J. J. Kopanski, K. P. Cheung, F. Zhang, C. Wang, J. P. Campbell, and J. S. Suehle, Appl. Phys. Lett. **98**, 233502 (2011).
[55]L. Dobaczewski, S. Bernardini, P. Kruszewski, P. K. Hurley, V. P. Markevich, I. D. Hawkins, and A. R. Peaker, Appl. Phys. Lett. **92**, 242104 (2008).
[56]M. A. Anders, P. M. Lenahan, and J. T. Ryan, Mater. Sci. Forum **1004**, 573 (2020).
[57]N. J. Harmon, S. R. McMillan, J. P. Ashton, P. M. Lenahan, and M. E. Flatte, IEEE Trans. Nucl. Sci. **67**, 1669 (2020).
[58]J. T. Ryan, A. Matsuda, J. P. Campbell, and K. P. Cheung, Appl. Phys. Lett. **106**, 163503 (2015).
[59]L. Militaru and A. Souifi, Appl. Phys. Lett. **83**, 2456 (2003).